Angewandte Chemie
Eine Zeitschrift der Gesellschaft Deutscher Chemiker

Supporting Information

Engineering Transport Properties in Interconnected Enargite-Stannite Type $Cu_{2+x}Mn_{1-x}GeS_4$ Nanocomposites

*V. Pavan Kumar, S. Passuti, B. Zhang, S. Fujii, K. Yoshizawa, P. Boullay, S. Le Tonquesse, C. Prestipino, B. Raveau, P. Lemoine, A. Paecklar, N. Barrier, X. Zhou, M. Yoshiya, K. Suekuni, E. Guilmeau**

Experimental Section

Synthesis

Polycrystalline samples of $Cu_{2+x}Mn_{1-x}GeS_4$ ($0 \leq x \leq 0.5$) were synthesized by mechanical-alloying followed by spark plasma sintering. All sample preparations and handling of powders were performed in an argon filled glovebox with oxygen content <1 ppm. Stoichiometric amounts of high purity elements Cu (99.9 %, Alfa Aesar), Mn (99.9 %, Alfa Aesar), Ge (99.999 %, Alfa Aesar), and S (99.99 %, Alfa Aesar) were loaded in a 25 mL tungsten carbide jar containing 7 balls of 10 mm under argon atmosphere. High-energy ball-milling was performed in a Fritsch Pulverisette 7 Premium line planetary ball-mill operating at room temperature (RT) at a disc rotation speed of 600 rpm during 12 h. The resulting powders were then ground and sieved down to 150 μm to remove large agglomerates. Powders were then loaded in graphite dies of 10 mm diameter and densified by spark plasma sintering (SPS-FCT HPD 25) at 873 K for 30 min under a pressure of 64 MPa (heating and cooling rate of 50 and 20 K min^{-1}, respectively). This produced 10 mm diameter pellets, ≈7 mm thick, with geometrical densities of around 95 %.

X-ray diffraction analysis

Powder X-ray diffraction (PXRD) data were recorded at room temperature using a Bruker D8 Advance Vario 1 two-circle diffractometer (θ-2θ Bragg-Brentano mode) using Cu-Kα1 radiation (λ = 1.540598 Å) equipped with a Ge(111) monochromator (Johansson type) and a Lynx Eye detector. Variable temperature X-ray powder diffraction data were collected guillon a Rigaku SmartLab diffractometer using a rotating anode with a Ge(111) monochromator (Cu Kα1 radiation, λ = 1.540598 Å, 45 kV, 200 mA) and an Anton Paar HTK1200N high-temperature chamber. The PXRD pattern were collected in Bragg-Brentano configuration with a HyPix-3000 detector between 300 and 650 K, every 25 K, under air with a heating rate of 10 °C min^{-1}.

Transmission electron microscopy and precession-assisted electron diffraction tomography

TEM images, high angle annular dark field (HAADF) images, selected area electron diffraction (SAED) and Electron Dispersive X-ray (EDX) spectroscopy analyses were collected on an electron microscope (Thermoscientific Talos F200S), at 200 kV. Samples of Cu_2MnGeS_4 and $Cu_{2.3}Mn_{0.7}GeS_4$ were prepared by ion-milling (Leica EM Res 102).

Precession-assisted electron diffraction tomography (PEDT)[1,2] data were obtained using a JEOL F200 (200 kV) transmission electron microscope (TEM) equipped with a ASI Cheetah M3 detector and a Nanomegas Digistar unit. Samples for TEM investigations were prepared by smoothly crushing powder under ethanol in an agate mortar and depositing drops of the mixture onto a holey carbon membrane supported by a Cu grid. PED patterns were collected using the Instamatic program[3] on two $Cu_{2+x}Mn_{1-x}GeS_4$ samples (x = 0 and 0.3) with a precession angle of 1.2° and a tilt step of about 1° between each pattern. PEDT data were processed using the programs PETS 2.0[4] and Jana2020.[5] Crystallographic details of data reduction and dynamical refinement results are given **Tables S1** and **1** for x = 0 and **Tables S2** and **2** for x = 0.3. Further details of the crystal structure investigations may be obtained from the joint CCDC/FIZ Karlsruhe online deposition service: https://www.ccdc.cam.ac.uk/structures/? by quoting the DOI of the article. 3D ED raw data will be deposited and findable in Zenodo NanED community (https://zenodo.org/communities/naned).

Stacking simulation

Based on the TEM study, it is possible to reevaluate the previously collected XRD pattern with a non-periodic approach, i.e. using the general recursion method for crystals containing coherent planar faults developed by Treacy *et al.*[6], implemented in DIFFaX and successor software FAULTS[7] used in the present work. Without entering into the calculation details, in such a method, the crystal is represented as a layered structure in which the layer sequence and their stacking vector are determined by a probabilistic law.

While for $x \leq 0.1$, it has been possible to modelize the stacking faults (see discussion in the article, **Figure 5 and 6**), for the samples with $x > 0.1$, the patterns become more complicated and are impossible to fit using the model applied for x = 0. If we focus on the right part of **Figure 2,** the peak around 29° gets more and more complex increasing x, with additional contributions. In both stannite and enargite, such reflection ((002) and (112) respectively) is directly related to the stacking period of the layers along the c axis. As a consequence, the appearance of new contributions means that new types of layers with smaller c axis should be introduced in the model. However, the introduction of a new set of layer types in the model, although mathematically feasible, appeared as "impracticable", since the introduction of a new

layer produces a set of new reflections generated by the mixing of the new layer with the previous ones, as can be noticed by the presence of several peaks in the range from 28.5 to 29.5°. Moreover, due to the complexity of the sample, it is possible to be composed of a mixture of slightly different defective crystallites or the presence of layers with different symmetry as in the case of enargite-luzonite equilibrium.[8]

From the application of the stacking fault model for $x = 0$ and $x = 0.1$ samples, it is possible to draw some conclusions also for the other samples. The ratio of intensities between the doublets at around 27° (enargite reflection (210) and (020)) and the peak around 28.6° (reflections (002) and (112) for enargite and stannite respectively) remains similar, meaning the fraction of the sample with the initial d-spacing stacking maintains the same equilibrium between stannite and enargite stacking. The decrease of the doublets at around 27° as a function of x is proportional to the increase of the peak at 29.2°, meaning that the new layers have a higher probability to stack in a stannite-like structure. At the light of the evolution with the temperature and microstructure analysis, the samples with $x > 0.1$ should be interpreted as the coexistence of two or more defective phases containing a mixture of stochiometric and Cu rich layers, and with preferentially Cu rich layer stacking in the stannite sequences.

Scanning electron microscopy

Scanning Electron Micrographs (SEM) and Electron Dispersive X-ray (EDX) spectroscopy analyses were collected using a JEOL JSM 7200F scanning electron microscope equipped with EDX X-Flash Bruker detector.

Electrical and thermal properties measurements:

The electrical resistivity (ρ) and Seebeck coefficient (S) were measured simultaneously from 2×3×10 mm^3 ingots, from 300 K up to 700 K using an ULVAC-ZEM3 instrument under partial helium pressure. A NETZSCH LFA-457 apparatus was used for measuring the thermal diffusivity under argon flow. The thermal conductivity (κ) was determined as the product of the geometrical density, the thermal diffusivity, and the theoretical heat capacity using the Dulong−Petit approximation. The lattice contribution to the thermal conductivity (κ_L) was determined by subtracting the estimated electronic component (κ_e) from the measured total thermal conductivity, κ. The electronic contribution, κ_e, was derived from the Wiedemann-

Franz law, $\kappa_e = L\sigma T$, where the Lorenz number, L, was approximated from the Seebeck coefficient using the simplified expression $L = 1.5 + \exp(-|S|/116)$. The estimated measurement uncertainties are 6% for the Seebeck coefficient, 8% for the electrical resistivity, 11% for the thermal conductivity, and 16% for the final figure of merit, ZT.[9] Note that ρ, S and κ were measured in the direction perpendicular to the SPS pressure direction.

Ab initio calculations

Total energy calculations and structure optimizations of tetragonal and orthorhombic Cu_2MnGeS_4 and their interfaces (stacking faults in orthorhombic phase, twin boundaries in tetragonal phases, coherent interfaces between orthorhombic and tetragonal phases shown in **Figure 8**) were performed using the plane-wave basis projector augmented wave (PAW) method[10] implemented in Vienna *Ab initio* Simulation Package (VASP).[11,12] The generalized gradient approximation (GGA) exchange-correlation functional of Perdew-Burke-Ernzerhof (PBE)[13,14] was employed. The valence configurations in the PAW potentials used in this study are $3d^{10}\ 4s^1$ for Cu, $3p^6\ 3d^5\ 4s^2$ for Mn, $3d^{10}\ 4s^2\ 4p^2$ for Ge and $3s^2\ 3p^4$ for S, with the rest electrons frozen as core electrons. The GGA + U scheme (Hubbard model)[15] was used to treat correlation effects in localized 3d orbitals in Cu and Mn. The values of U were set to 4.2 and 3.9 eV for Cu and Mn, respectively, to well reproduce the electronic density of states (DOS) obtained using the hybrid functional HSE06.[16,17] Atomic positions and lattice constants were optimized with the criteria of total energy convergence of 1.0×10^{-6} eV/cell and atomic residual force of 5.0×10^{-3} eV/Å. A plane-wave energy cutoff was set to 420 eV. The first Brillouin-zone was sampled using Γ-centered k-point grids of 6 × 6 × 3, 4 × 4 × 5 and 4 × 5 ×1 for tetragonal Cu_2MnGeS_4, orthorhombic Cu_2MnGeS_4, and their interface models, respectively. For the electronic DOS calculations, finer Γ-centered k-point grids of 12 × 12 × 6, 8 × 8 × 10, and 8 × 10 × 2 were used, respectively. We also investigated the electronic DOS of $Cu_{2.5}Mn_{0.5}GeS_4$ by substituting one Mn by one Cu in the unit cell of Cu_2MnGeS_4, with the same computational conditions written above. The interface energy, ΔE_{intf}, which indicates the energy difference between the interface and the bulk crystal, are defined as follows:

$$\Delta E_{\mathrm{intf}} = \frac{E_{\mathrm{intf}} - \frac{N_{\mathrm{intf}}}{N_{\mathrm{bulk}}} E_{\mathrm{bulk}}}{2A}, \qquad (1)$$

where E_{intf} and E_{bulk} are the internal energies of the interface model and the unit cell of Cu_2MnGeS_4, N_{intf} and N_{bulk} are the number of atoms in the interface model and the unit cell, and A is the cross-sectional area of the interface. ΔE_{intf} is divided by two to account for the two identical interfaces in the supercell to satisfy the three-dimensional periodic boundary conditions.

Phonon calculations

Phonon properties and lattice thermal conductivity were calculated using the Parlinski-Li-Kawazoe method[18] as implemented in Phonopy[19] and Phono3py.[20] The second-order and third-order interatomic force constants were derived from the forces obtained from *ab initio* calculations using the supercells with dimensions of approximately 10 Å or larger. The magnitude of atomic displacements for these calculations are set to 0.01 and 0.03 Å, respectively. Phonon band structures, phonon DOS, and group velocities were calculated within the harmonic approximation using dense q-point meshes of ~2,000 grid/Å^{-3}. κ_L was calculated only for the bulk of tetragonal and orthorhombic Cu_2MnGeS_4 by solving the Boltzmann transport equation with the single-mode relaxation-time approximation, with q-point meshes of 19 × 19 × 11 and 11 × 11 × 17, respectively. Note that huge computational cost prevented us from calculating κ_L for the interface models.

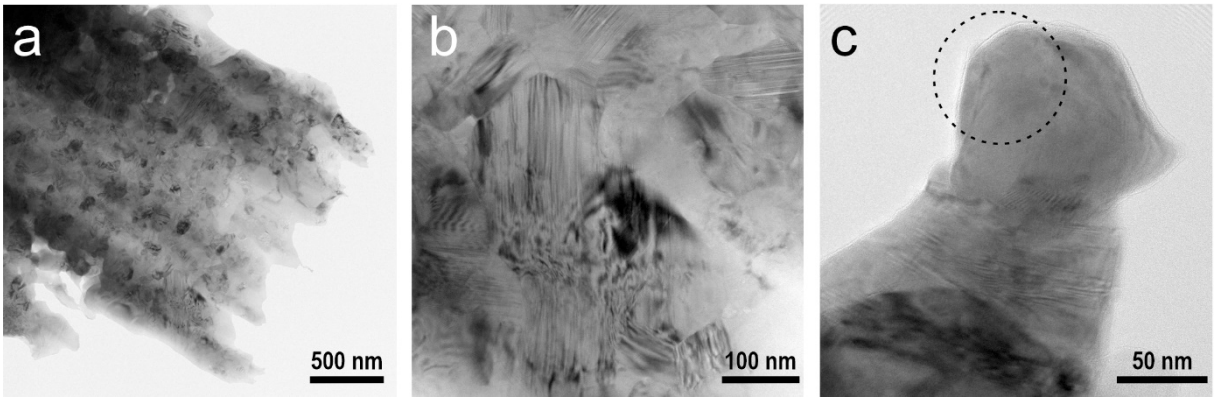

Figure S1. Bright field TEM images of Cu_2MnGeS_4 showing in a) and b) the fine grain size and in b) the recurrent presence of a stripe-like contrast within grains. In c) the typical size of area explore by PEDT is highlighted with a dashed circle.

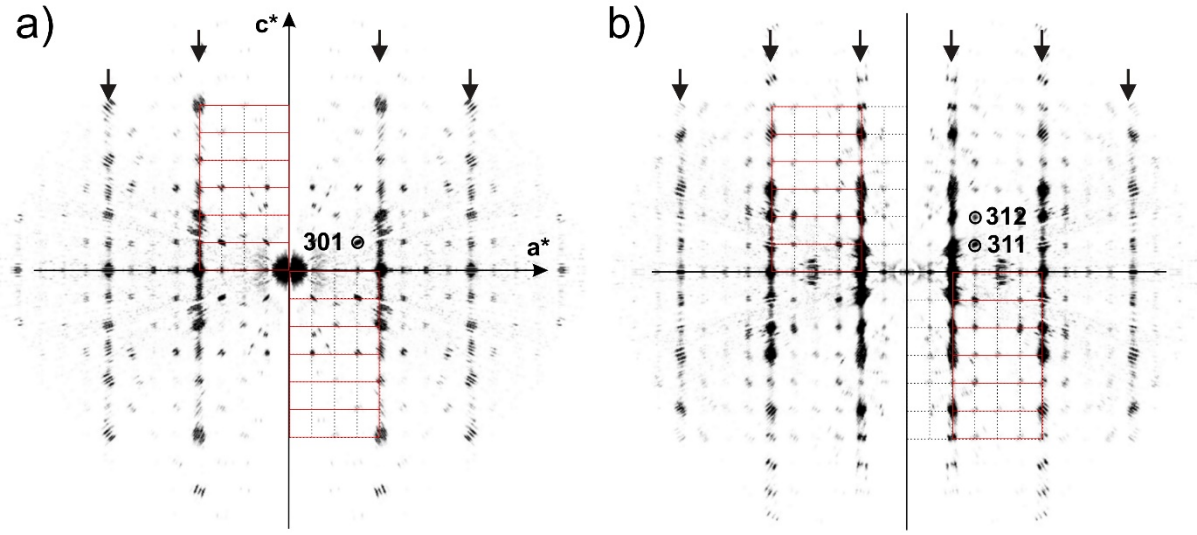

Figure S2: Reciprocal space sections reconstructed from PEDT data for the sample Cu_2MnGeS_4 with in: a) *h0l* section and b) *h1l*. The more intense reflections, related to the wurtzite subcell, are highlighted using red lines while weaker reflections, characterizing enargite, are highlighted using black dotted lines.

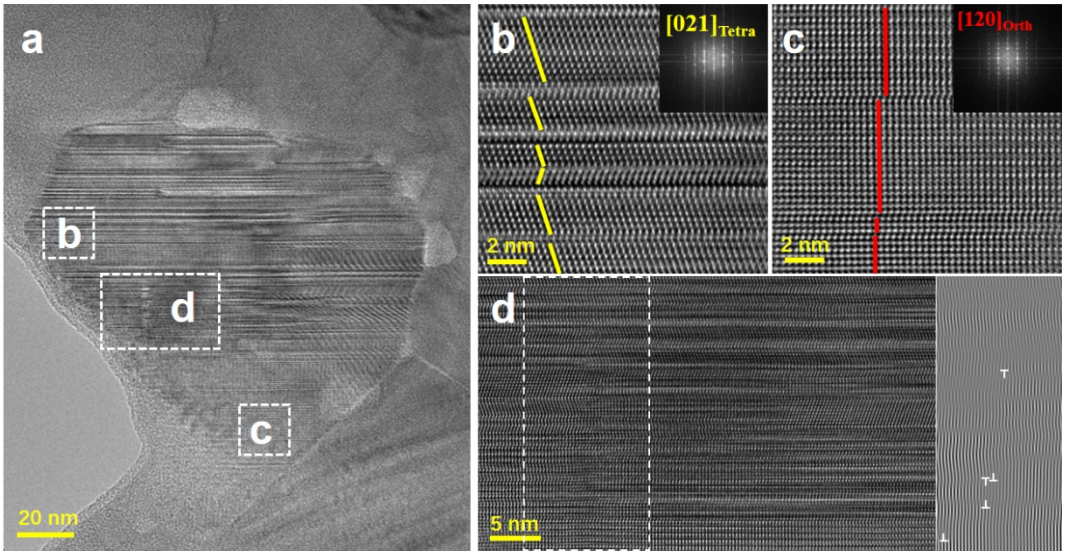

Figure S3. HRTEM images of Cu_2MnGeS_4. (b-d) the enlarged views correspond to the dotted regions in (a). (b, c) show that plenty of the nanotwins and planar defects, e.g., stacking faults, exist in orthorhombic and tetragonal phases. d) Besides the coexistence of orthorhombic and tetragonal phases with dense coherent interfaces and planar defects, there are dislocations in the boundaries (as indicated in the filtered HRTEM image at the right panel of d) and lattice distortions in local areas which should result in local disorder.

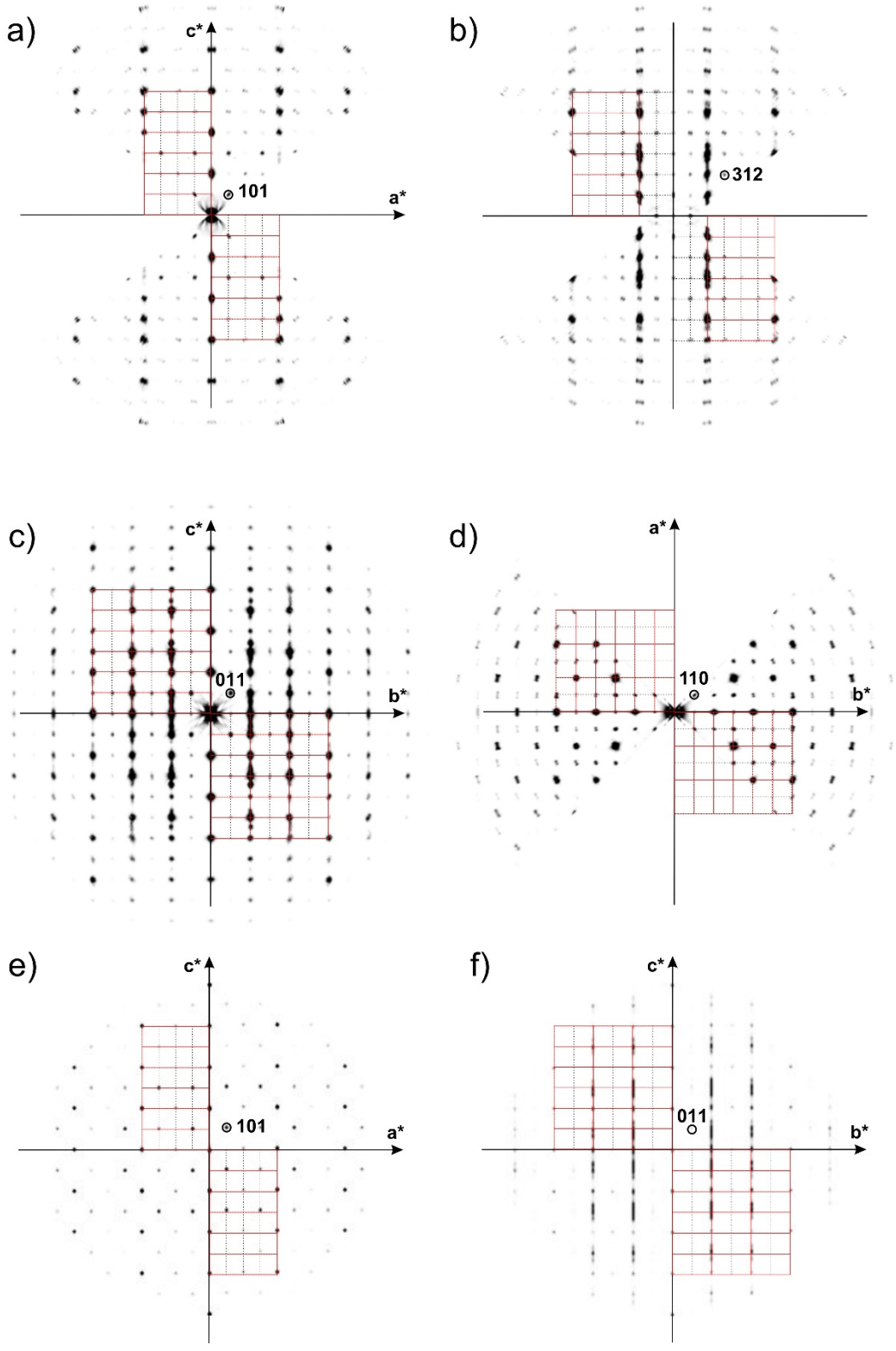

Figure S4. Reciprocal space sections reconstructed from PEDT data for the sample $Cu_{2+x}Mn_{1-x}GeS_4$ ($x = 0.3$ phase 1: enargite) with in: a) *h0l* section, b) *h1l*, c) *0kl* section and d) *hk*0 section. The more intense reflections, related to the wurtzite subcell, are highlighted using red lines while weaker reflections, characterizing enargite, are highlighted using black dotted lines. Part e) and f) reciprocal space sections calculated from the model refined by powder diffraction.

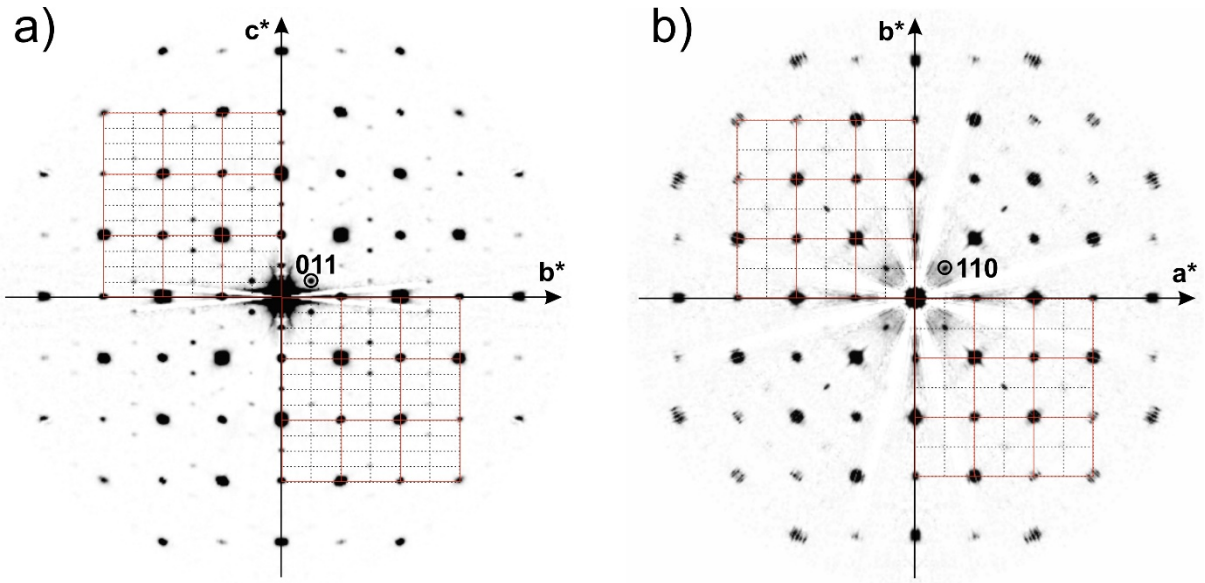

Figure S5. Reciprocal space sections reconstructed from PEDT data for the sample $Cu_{2+x}Mn_{1-x}GeS_4$ (x = 0.3 phase 2: stannite) with in: a) 0kl section and b) hk0 section. The more intense reflections, related to the sphalerite subcell, are highlighted using red lines while weaker reflections, characterizing stannite, are highlighted using black dotted lines.

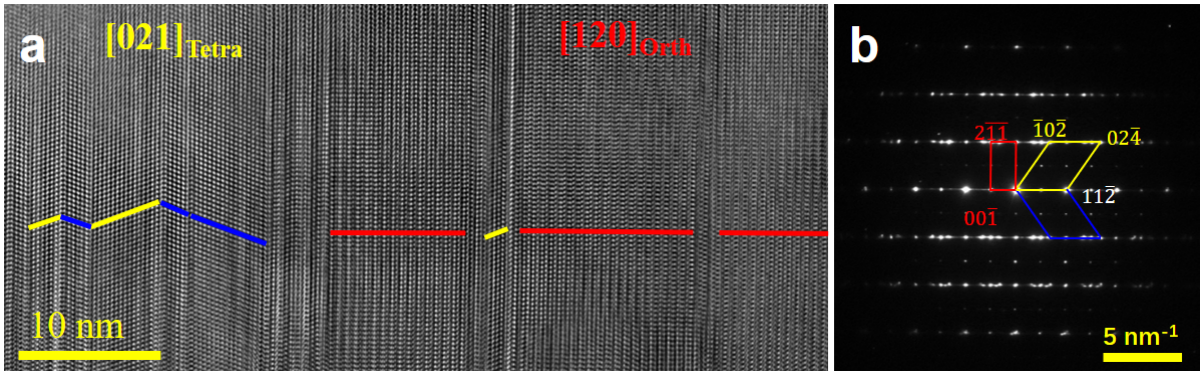

Figure S6. a) HRTEM image and b) SAED pattern of $Cu_{2.3}Mn_{0.7}GeS_4$ along the direction where the lattice significant difference coherent interfaces formed between the enargite and stannite structures. The HRTEM image was obtained from the same grain of **Figure 3(a, b)** but different regions and along the same direction. While when the grain rotates ~30° along the direction parallel to the coherent interface, a single-crystal-like feature appears (see **Figure 4a**).

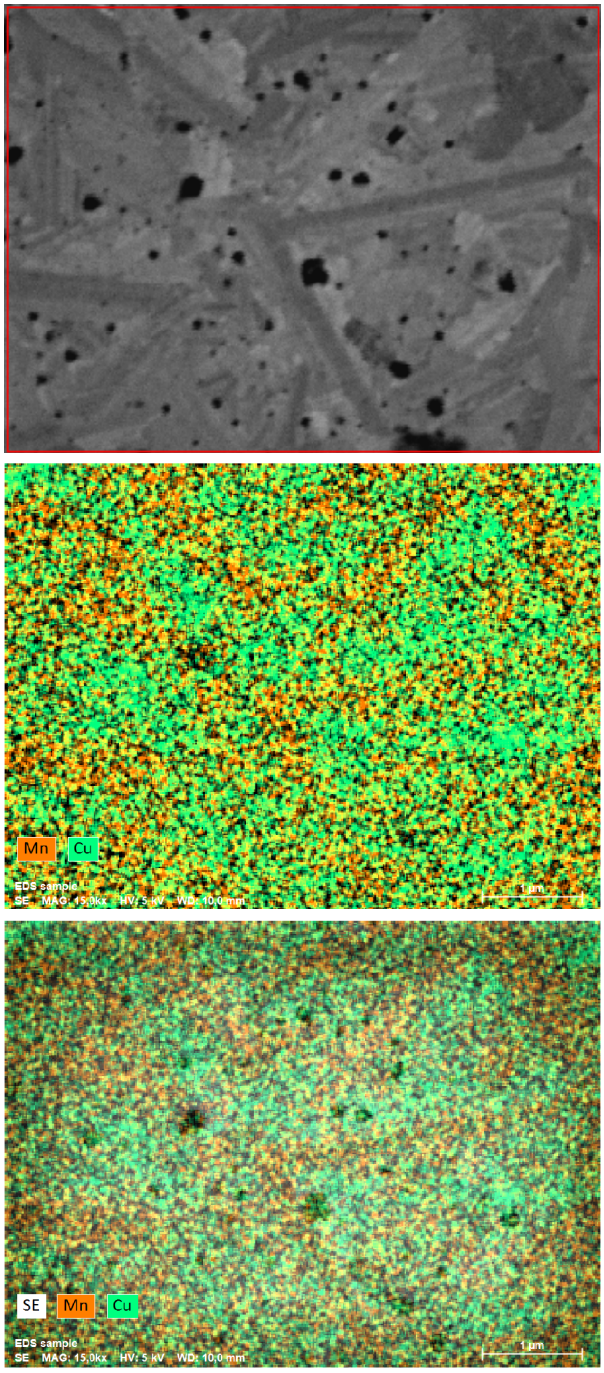

Figure S7. SEM micrographs and EDS mapping of $Cu_{2.3}Mn_{0.7}GeS_4$ sample.

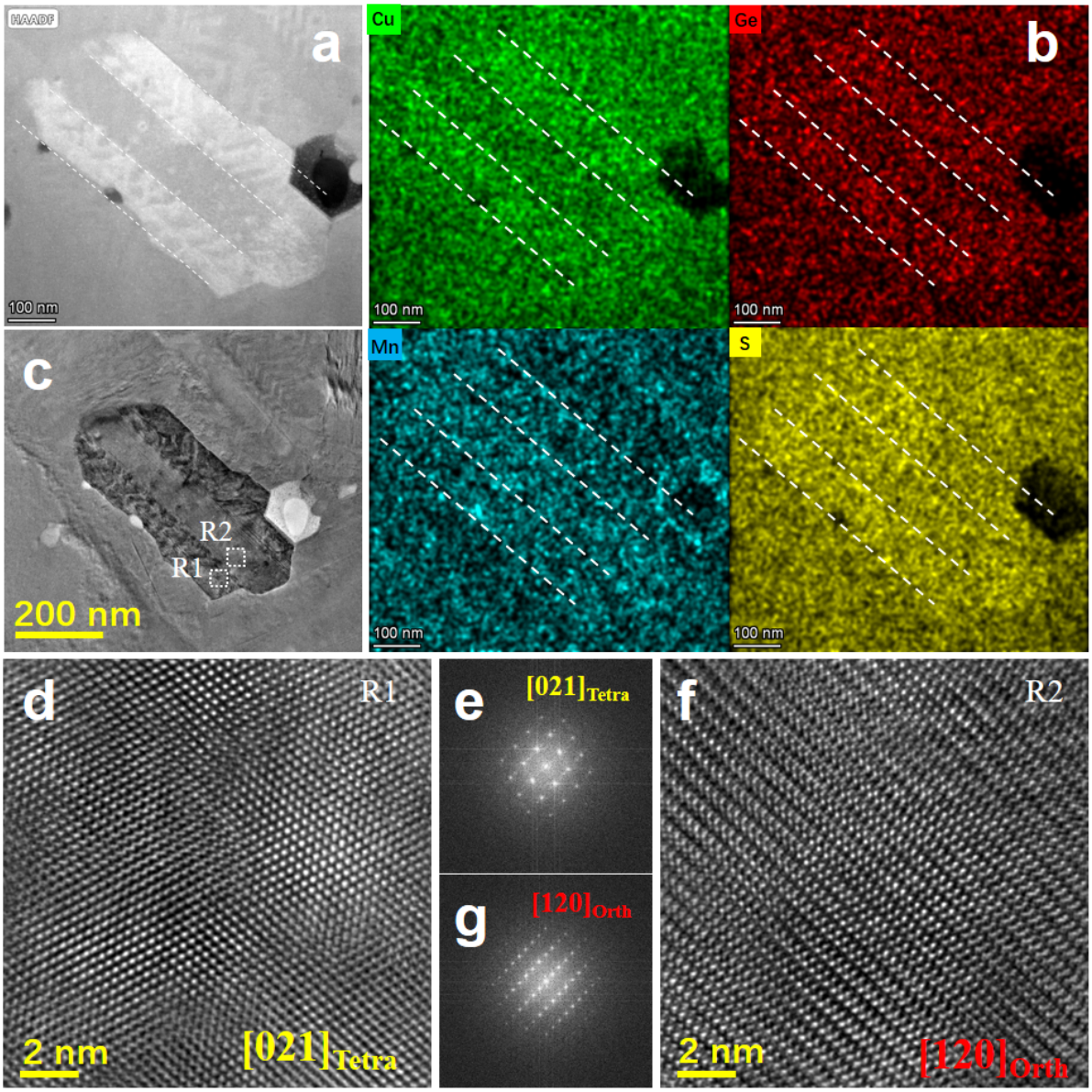

Figure S8. Microstructure characterization of $Cu_{2.3}Mn_{0.7}GeS_4$ sample. (a, b) STEM-HAADF and the corresponding EDS mapping around the elongated grain show enrichment of Cu and Ge in the two bright lamellas (as indicated by the dotted lines) and relatively Mn-rich in the middle dark grey lamella. The chemical composition was determined as $Cu_{2.40}Mn_{0.76}Ge_{0.77}S_4$, $Cu_{2.19}Mn_{0.88}Ge_{0.74}S_4$, $Cu_{2.65}Mn_{0.78}Ge_{0.82}S_4$ for the three lamellas from lower left to the upper right side. (d, f) the HRTEM images from the dotted regions of c. Since Mn(25) has lighter atomic number than that of Cu(29) and Ge(32), thus the Mn-rich lamella shows dimmer contrast in the Z-contrast (i.e., HAADF) image (a) as expected. The HRTEM images and corresponding FFT patterns indicate that Cu-rich lamella has tetragonal structure while Mn-rich elongated grain possesses orthorhombic phase.

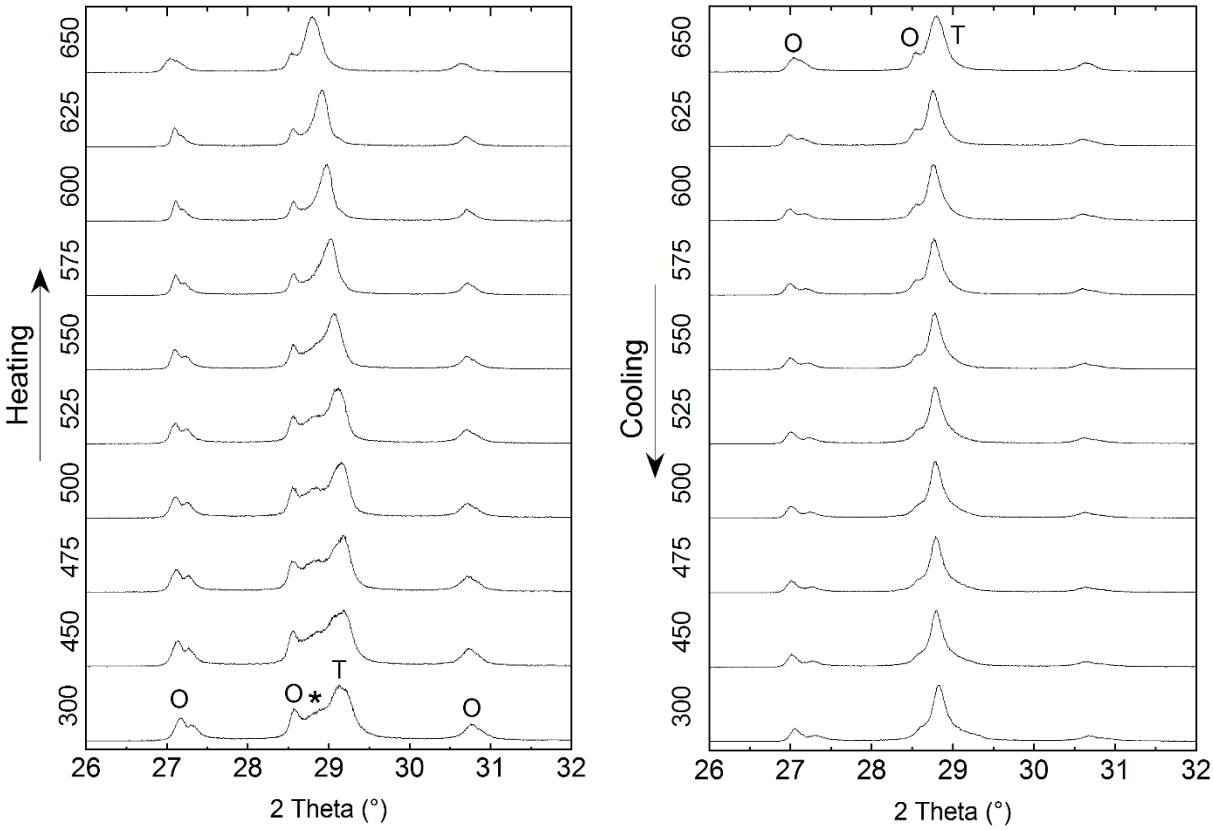

Figure S9. XRD patterns of $Cu_{2.3}Mn_{0.7}GeS_4$ in the temperature range 300 – 650 K during heating and cooling cycles. O: orthorhombic; T: tetrognal, *additional contribution.

From RT to 525 K, the PXRD patterns remains almost similar, which means that no reaction occurs between the tetragonal and orthorhombic phases. From 550 K to 650 K, the intensities of the diffraction peaks of the orthorhombic phase do not vary significantly, while the main diffraction peak of the tetragonal phase tends to narrow and to shift to lower angles, at the expense of the additional contribution observed around 28.8° (see discussion in the second paragraph of the structural analysis section). This supports the hypothesis that this contribution is likely related to the new types of layers with smaller *c axes*. When heating up the sample, the chemical composition homogeneity increases and the microstructural disorder decreases leading to the formation of only one tetragonal phase, with better crystallinity and larger cell parameter resulting from the homogeneous mix of stochiometric and Cu rich layers. When cooling down the sample from 650 K to RT, the content of the orthorhombic phase tends to slightly decrease, but remains still present at RT. At the same time, the main diffraction peak of the tetragonal phase is slightly broadening. All those phenomena appearing along the heating

and cooling ramps confirm the complexity of the crystal chemistry in sphalerite and wurzite-type copper-based sulfides. It clearly indicates that the stability of those interconnected enargite-stannite type domains is not only related to the initial composition but also to the thermal treatments. In the present case, the powders being prepared by mechanical-alloying at low temperature followed by SPS process with fast heating and cooling ramps, it leads to an out-of-equilibrium state where the more stable phase is not yet fully crystallized. Further investigations are ongoing to understand the key parameters which control the formation of those enargite- or stannite-type phases.

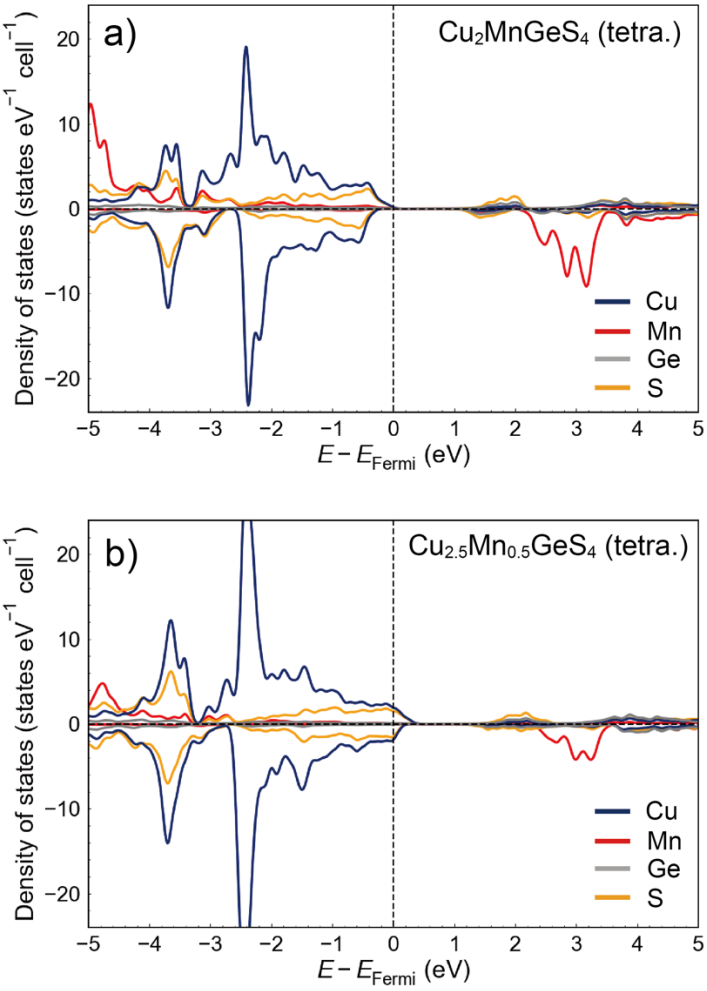

Figure S10. Element-deconvoluted electronic density of states (DOS) of (a) tetragonal Cu_2MnGeS_4 and (b) $Cu_{2.5}Mn_{0.5}GeS_4$. E_{Fermi} is the Fermi energy. Positive and negative DOS indicate the partial DOS of up-spin and down-spin orbitals, respectively.

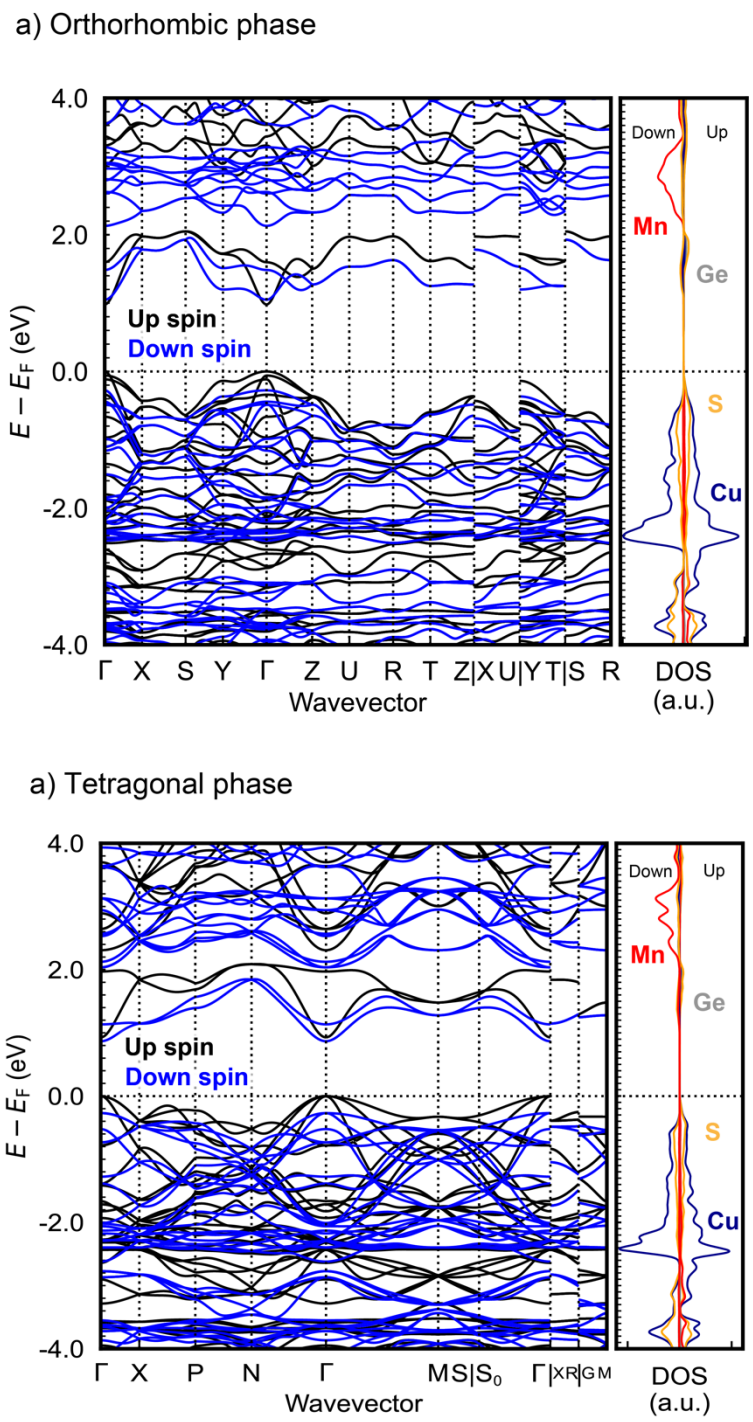

Figure S11. Electronic band structures for (a) orthorhombic and (b) tetragonal Cu_2MnGeS_4 phases with the element-deconvoluted electronic density of states (DOS) along these special *k*-points. E_F is the Fermi energy.

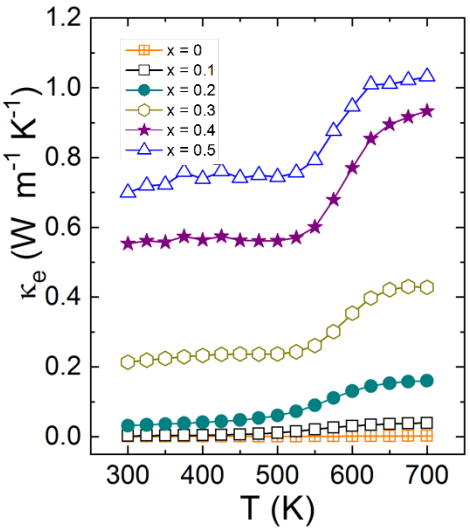

Figure S12. Electronic contribution to the thermal conductivity in the in the $Cu_{2+x}Mn_{1-x}GeS_4$ series.

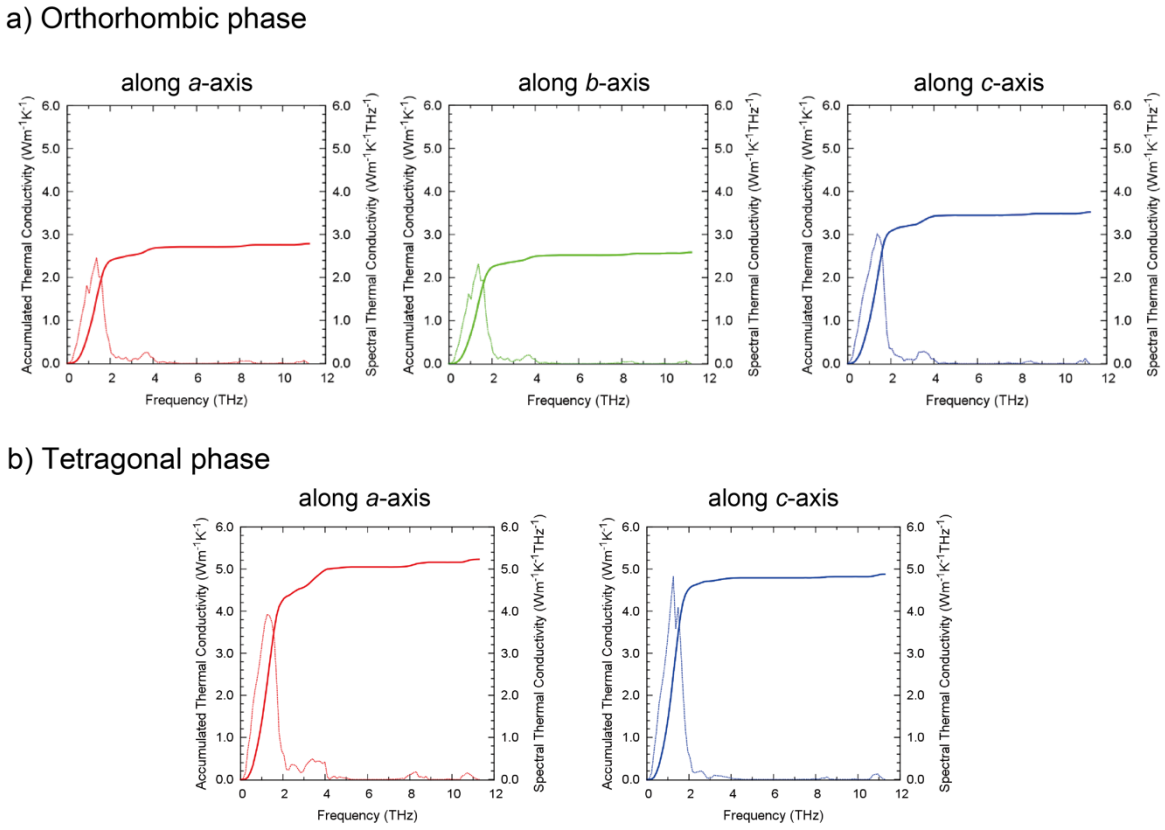

Figure S13. Spectral (dotted) and accumulated (solid) lattice thermal conductivities at 300 K as a function of phonon frequency for (a) orthorhombic enargite-type and (b) tetragonal stannite-type phases, along each axis (see **Fig. 1** for the conventional cells).

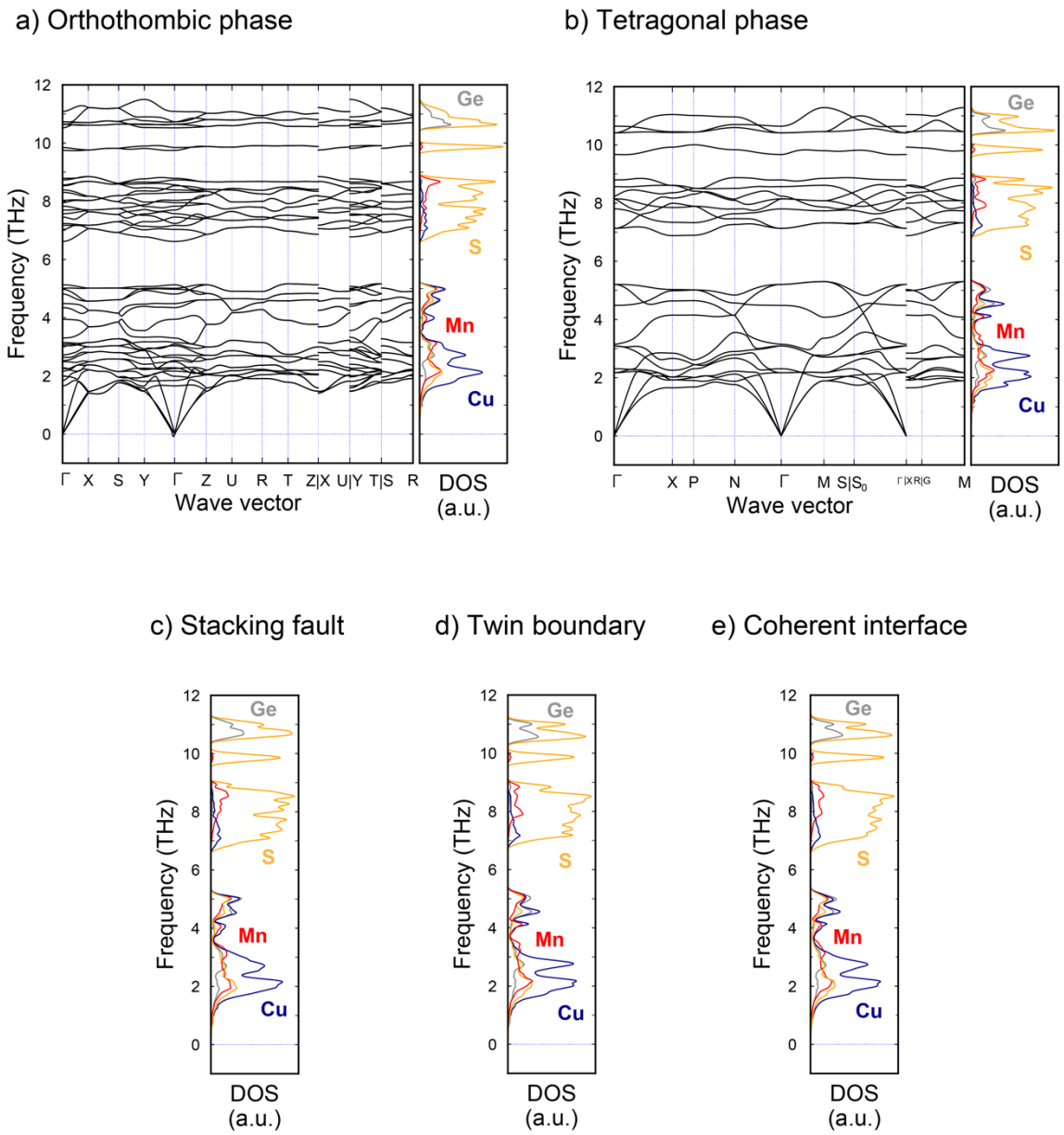

Figure S14. Phonon band structures and DOS of (a) orthorhombic enargite-type and (b) tetragonal stannite-type phases. Phonon DOS of (c) the orthorhombic enargite-type phase with stacking faults, (d) the tetragonal stannite-type phase with twin boundaries, and (e) the orthorhombic enargite-type and tetragonal stannite-type phases with coherent interfaces in-between. See **Fig. 8** for the structures of the interface models.

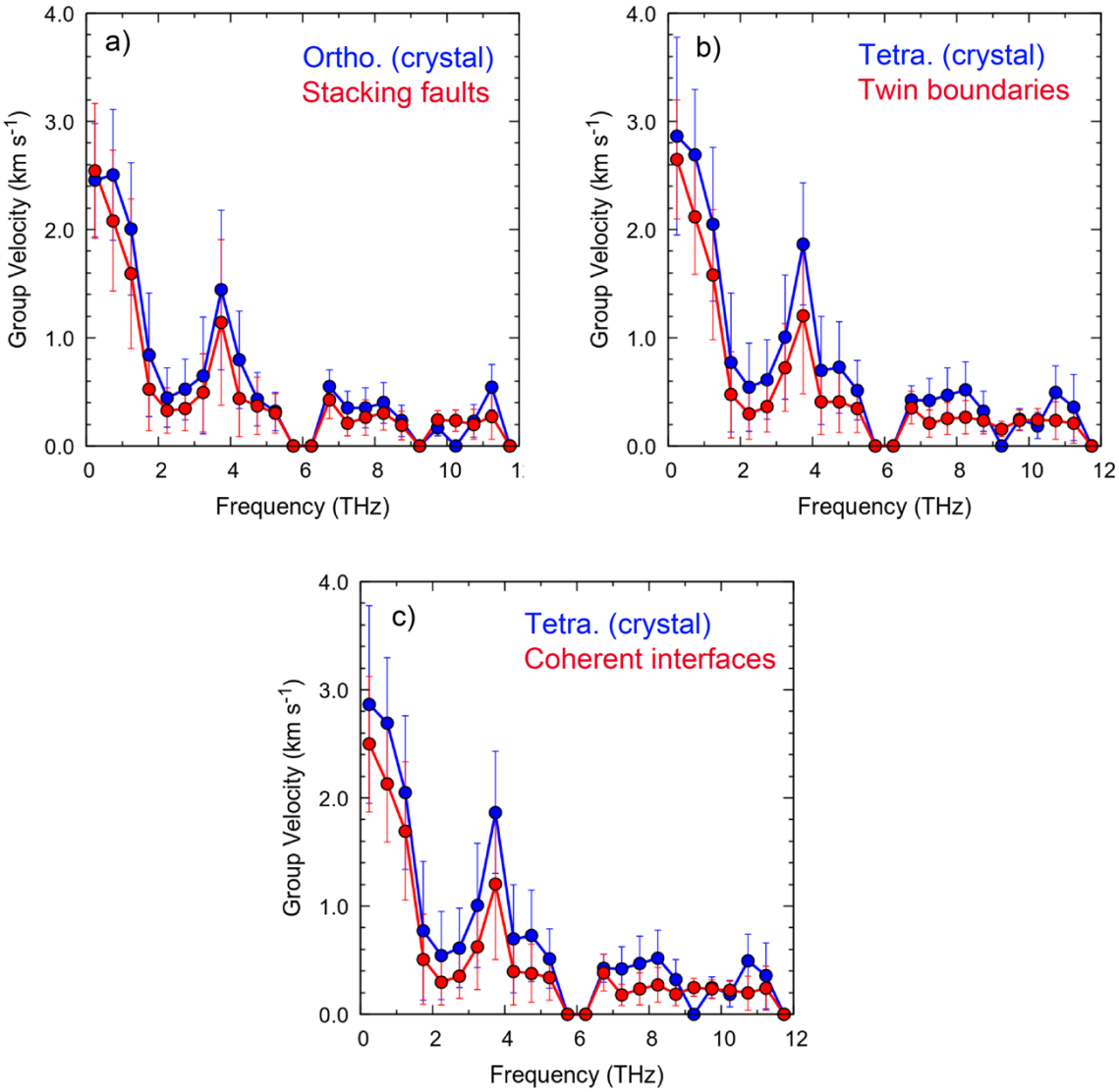

Figure S15. Averaged phonon group velocities calculated for 0.5 THz frequency windows for (a) the orthorhombic enargite-type phase and the stacking faults, (b) the tetragonal stannite-type phase and the twin boundaries, and (c) the tetragonal stannite-type phases and the coherent interfaces. Standard deviations of the group velocities are shown as bars. See **Fig. 8** for the structures of the interface models.

Table S1: Crystallographic details of data reduction and dynamical refinement obtained for the orthorhombic phase observed in the sample Cu_2MnGeS_4.

Structure type	Enargite
Temperature (K)	293
Crystal system, space group	Orthorhombic, $Pmn2_1$ (SG : 31)
a, b, c (Å)	7.69(1), 6.541(7), 6.340(9)
V (Å^3)	318.9
Electron wavelength λ (Å)	0.0251
Number of frames	88
Tilt range (°)	87.7
Precession angle (°)	1.2
Resolution $\sin(\theta_{max})/\lambda$ (Å^{-1})	0.85
Cumulative coverage (%)	89.5
Measured, observed[$I>3\sigma(I)$] reflections	3682, 2342
No. of refined parameters, restraints	100, 0
g_{max} (Å^{-1}), $S_{g,max}$ (Å^{-1}), R_{Sg}, steps	1.9, 0.01, 0.4, 128
R(obs), R(all), wR(all), GoF(all)	0.142, 0.183, 0.179, 6.9

Table S2: Crystallographic details of data reduction and dynamical refinement obtained for the two phases observed in the sample $Cu_{2+x}Mn_{1-x}GeS_4$ (x = 0.3).

Structure type	Phase 1: Enargite	Phase 2: Stannite
Temperature (K)	293	293
Crystal system, space group	Orthorhombic, $Pmn2_1$ (SG : 31)	Tetragonal, I-42m (SG: 121)
a, b, c (Å)	7.634(6), 6.558(3), 6.238(3)	5.393(6), 5.393(6), 10.44(1)
V (Å^3)	312.3	303.6
Electron wavelength λ (Å)	0.0251	0.0251
Number of frames	102	99
Tilt range (°)	100.5	97.5
Precession angle (°)	1.2	1.2
Resolution $\sin(\theta_{max})/\lambda$ (Å^{-1})	1.00	0.90
Cumulative coverage (%)	82.2	100
Measured, observed[$I>3\sigma(I)$] reflections	7212, 4753	2041, 916
No. of refined parameters, restraints	115, 0	78, 0
g_{max} (Å^{-1}), $S_{g,max}$ (Å^{-1}), R_{Sg}, steps	2.2, 0.01, 0.4, 256	2.0, 0.01, 0.4, 256
R(obs), R(all), wR(all), GoF(all)	0.130, 0.160, 0.157, 5.6	0.129, 0.157, 0.160, 7.8

Table S3. Atomic parameters obtained for the sample $Cu_{2+x}Mn_{1-x}GeS_4$ (x = 0.3) based on the structure refinements against PEDT data (**Table S2**). A stoichiometry corresponding to Cu_2MnGeS_4 was imposed for both phases (see text for further comments about this). Site occupancy are all equal to 1. The BVS column gives the bond valence sums obtained for each atomic position.

Phase 1: Enargite Pmn2_1 a = 7.634(6) Å, b = 6.558(3) Å *and* c = 6.238(3) Å

Atom label	x	y	z	Uiso (Å²)	BVS
Ge1	0.5	0.8259(2)	0.2574(3)	0.0054(3)	4.03(2)
Mn1	0	0.8402(3)	0.2587(3)	0.0120(4)	2.03(1)
Cu1	0.2512(2)	0.3241(2)	0.25*	0.0142(3)	1.12(1)
S1	0.2633(4)	0.6620(3)	0.3800(4)	0.0094(4)	2.05(1)
S2	0	0.1889(4)	0.4030(4)	0.0088(5)	2.13(1)
S3	0.5	0.1491(4)	0.3647(4)	0.0072(5)	2.08(1)

* *fixed parameter (polar space group)*

Phase 2: Stannite I-42*m* a = 5.393(6) Å and c = 10.44(1) Å

Atom label	x	y	z	Uiso (Å²)	BVS
Ge1	0.5	0.5	0.5	0.0106(6)	3.77(1)
Mn1	0	0	0.5	0.0134(7)	2.34(1)
Cu1	0.5	0	0.75	0.0070(4)	1.22(1)
S1	0.7382(2)	0.7382(2)	0.6274(2)	0.0096(4)	2.14(1)

Table S4. Atomic parameters and stacking probability obtained for the Faults fitting of sample Cu_2MnGeS_4. The phase is simulated using the four possible layers represented in the top line of **Figure 5**.

*layer 1: P*1 a = 7.6112(2) Å, b = 6.5356(2) Å and c = 3.1198(1) Å

R-Factor = 4.1 Chi^2 = 1.83

Atom label	x	y	z	Biso (Å²)
Ge1	0.5	0.827(2)	0.833(9)	1.56(2)
Mn1	0	0.8405(3)	0.2585(4)	1.56(2)
Cu1	0.2501(1)	0.324	0.82	1.56(2)
Cu1	0.7499(1)	0.324	0.82	1.56(2)
S1	0.2368(4)	0.6612(3)	0.3792(4)	1.56(2)
S2	0.763(4)	0.1876(4)	0.4010(4)	1.56(2)
S3	0.5	0.816(4)	0.118(7)	1.56(2)
S4	0	0.850(5)	0.051(7)	1.56(2)

transition	probability	Stacking vector		
		x	y	z
stannite → stannite	0.848(2)	½	⅓	0.9902(3)
stannite → enargite	0.152(2)	½	-⅓	0.9902(3)
enargite → enargite	0.9490(3)	½	-⅓	1
enargite → stannite	0.0339(2)	½	⅓	0.9902(3)
enargite → enargite + SF	0.0170(3)	½	⅓	1

Table S5. Averaged value of squared group velocity $\overline{v^2}$ for acoustic phonons with frequencies less than 1.5 THz. The reduction from the corresponding crystal structure is also shown for each interface. The interface models used for these calculations are shown in **Fig. 8**.

	$\overline{v^2}$ (m^2/s^2)	Reduction (%)
Orthorhombic enargite-type structure (crystal)	4.89	-
Tetragonal stannite-type structure (crystal)	5.35	-
Stacking faults in the ortho. phase	3.54	27.6
Twin boundaries in the tetra. phase	3.36	37.2
Coherent boundaries between the orthorhombic and tetragonal phases	3.71	27.5

References

(1) Mugnaioli, E.; Gorelik, T.; Kolb, U. "Ab Initio" Structure Solution from Electron Diffraction Data Obtained by a Combination of Automated Diffraction Tomography and Precession Technique. *Ultramicroscopy* **2009**, *109* (6), 758–765.

(2) Boullay, P.; Palatinus, L.; Barrier, N. Precession Electron Diffraction Tomography for Solving Complex Modulated Structures: The Case of $Bi_5Nb_3O_{15}$. *Inorg. Chem.* **2013**, *52* (10), 6127–6135.

(3) Smeets, S.; Wang, B. Instamatic (V.1.7.0), Zenodo, Https://Doi.Org/10.5281/Zenodo.1090388. *Instamatic (V.1.7.0), Zenodo, https://doi.org/10.5281/zenodo.1090388*.

(4) Palatinus, L.; Brázda, P.; Jelínek, M.; Hrdá, J.; Steciuk, G.; Klementová, M. Specifics of the Data Processing of Precession Electron Diffraction Tomography Data and Their Implementation in the Program PETS2.0. *Acta Crystallogr. B* **2019**, *75*, 512.

(5) Petříček, V.; Dušek, M.; Palatinus, L. Crystallographic Computing System Jana2006: General Features. *Zeitschrift fur Krist.* **2014**, *229*, 345.

(6) Treacy, M. M. J.; Newsam, J. M.; Deem, M. W. A General Recursion Method for Calculating Diffracted Intensities from Crystals Containing Planar Faults. *Proc. R. Soc. London. Ser. A Math. Phys. Sci.* **1991**, *433* (1889), 499–520.

(7) Casas-Cabanas, M.; Reynaud, M.; Rikarte, J.; Horbach, P.; Rodr\'\iguez-Carvajal, J. *FAULTS*: A Program for Refinement of Structures with Extended Defects. *J. Appl. Crystallogr.* **2016**, *49* (6), 2259–2269.

(8) Pósfai, M.; Sundberg, M. Stacking Disorder and Polytypism in Enargite and Luzonite. *Am. Mineral.* **1998**, *83* (3–4), 365–372.

(9) Alleno, E.; Bérardan, D.; Byl, C.; Candolfi, C.; Daou, R.; Decourt, R.; Guilmeau, E.; Hébert, S.; Hejtmanek, J.; Lenoir, B.; Masschelein, P.; Ohorodnichuk, V.; Pollet, M.; Populoh, S.; Ravot, D.; Rouleau, O.; Soulier, M. A Round Robin Test of the Uncertainty on the Measurement of the Thermoelectric Dimensionless Figure of Merit of $Co_{0.97}Ni_{0.03}Sb_3$. *Rev. Sci. Instrum.* **2015**, *86*, 011301.

(10) Blöchl, P. E. Projector Augmented-Wave Method. *Phys. Rev. B* **1994**, *50* (24), 17953–17979.

(11) Kresse, G.; Hafner, J. Ab Initio Molecular-Dynamics Simulation of the Liquid-Metal--Amorphous-Semiconductor Transition in Germanium. *Phys. Rev. B* **1994**, *49* (20), 14251–14269.

(12) Kresse, G.; Furthmüller, J. Efficient Iterative Schemes for Ab Initio Total-Energy Calculations Using a Plane-Wave Basis Set. *Phys. Rev. B* **1996**, *54* (16), 11169–11186.

(13) Perdew, J. P.; Burke, K.; Ernzerhof, M. Generalized Gradient Approximation Made Simple. *Phys. Rev. Lett.* **1996**, *77* (18), 3865–3868.

(14) Perdew, J. P.; Burke, K.; Ernzerhof, M. Generalized Gradient Approximation Made Simple - ERRATUM. *Phys. Rev. Lett.* **1997**, *78* (7), 1396.

(15) Dudarev, S. L.; Botton, G. A.; Savrasov, S. Y.; Humphreys, C. J.; Sutton, A. P. Electron-Energy-Loss Spectra and the Structural Stability of Nickel Oxide: An

LSDA+U Study. *Phys. Rev. B* **1998**, *57* (3), 1505–1509.

(16) Heyd, J.; Scuseria, G. E.; Ernzerhof, M. Hybrid Functionals Based on a Screened Coulomb Potential. *J. Chem. Phys.* **2003**, *118* (18), 8207–8215.

(17) Krukau, A. V; Vydrov, O. A.; Izmaylov, A. F.; Scuseria, G. E. Influence of the Exchange Screening Parameter on the Performance of Screened Hybrid Functionals. *J. Chem. Phys.* **2006**, *125* (22), 224106.

(18) Parlinski, K.; Li, Z. Q.; Kawazoe, Y. First-Principles Determination of the Soft Mode in Cubic ZrO_2. *Phys. Rev. Lett.* **1997**, *78* (21), 4063–4066.

(19) Togo, A.; Tanaka, I. First Principles Phonon Calculations in Materials Science. *Scr. Mater.* **2015**, *108*, 1–5.

(20) Togo, A.; Chaput, L.; Tanaka, I. Distributions of Phonon Lifetimes in Brillouin Zones. *Phys. Rev. B* **2015**, *91* (9), 94306.